



$\alpha\text{-Fe}_2\text{O}_3$ /single-walled carbon nanotube hybrid films as high-performance anodes for rechargeable lithium-ion batteries

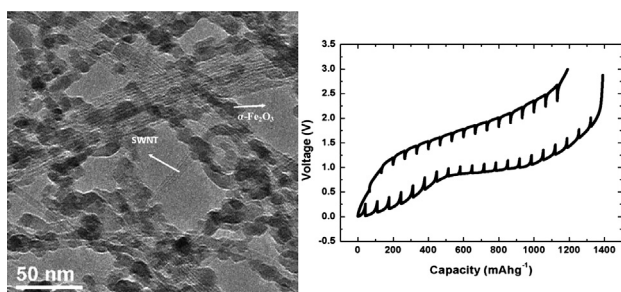


Zeyuan Cao, Bingqing Wei*

Department of Mechanical Engineering, University of Delaware, Newark, DE 19716, United States

HIGHLIGHTS

- $\alpha\text{-Fe}_2\text{O}_3$ /SWNT hybrid films were synthesized by a simple heat treatment method.
- The hybrid films as anodes exhibit a high specific capacity over 1000 mAh g⁻¹.
- Excellent cyclic stability up to 100 cycles was achieved from the hybrid films.
- The hybrid film thickness has a significant impact on Li⁺ diffusion coefficient.

GRAPHICAL ABSTRACT**ARTICLE INFO****Article history:**

Received 24 March 2013

Received in revised form

21 April 2013

Accepted 22 April 2013

Available online 30 April 2013

Keywords: $\alpha\text{-Fe}_2\text{O}_3$

Single-walled carbon nanotubes

Hybrid films

Lithium-ion batteries

Anodes

Diffusion coefficient

ABSTRACT

The hybrid films composed of single-walled carbon nanotube (SWNT) macro-films and $\alpha\text{-Fe}_2\text{O}_3$ nanoparticles in fine crystalline size (6–20 nm) are prepared by a simple heat treatment of the as-synthesized SWNT macro-films. The SWNT macro-films with superior conductivity and flexibility can facilitate the charge transfer processes as well as accommodate the volumetric change of the $\alpha\text{-Fe}_2\text{O}_3$ nanoparticles due to the Li-intercalated phase transformations, enabling high specific capacities over 1000 mAh g⁻¹ and an excellent cyclic stability up to 100 cycles for the $\alpha\text{-Fe}_2\text{O}_3$ /SWNT hybrid films. The increment of the capacity to approach the theoretical capacity of $\alpha\text{-Fe}_2\text{O}_3$ during cycling results from the relaxed conversional reactions between the reduced and oxidized states of iron ions (Fe^0 , Fe(II) and Fe(III)). Experimental results have shown that the thickness of the hybrid films has a significant impact on the diffusion coefficient of Li⁺. With a thickness comparable to Li⁺ characteristic diffusion length in the range of 300–500 nm, the hybrid films exhibit an optimal electrochemical performance. The findings on the synthesis approach and the thickness effect provide a promising strategy for a large-scale production of high-performance anode materials for Li-ion batteries.

© 2013 Elsevier B.V. All rights reserved.

1. Introduction

The development of rechargeable lithium-ion batteries (LIBs) with a higher energy density and a longer lifetime is the research focus as well as the bottleneck for large-scale applications of electric vehicles and portable electronics [1,2]. Seeking alternatively potential anode and cathode materials becomes increasingly

important and urgent to meet the ever-growing demands of high energy density LIBs, especially with the popularization of the highly power-consuming smart phones [2]. Nanostructured transition metal oxides ($M_x\text{O}_y$) have been extensively studied as the candidates for LIB anodes because of their shortening diffusion paths for lithium ions and high theoretical specific capacities, resulting not only from the intercalation/deintercalation mechanism but also from reversible conversion reactions to produce metal nanoparticles M^0 and Li_2O with excess of over 6 moles of Li⁺ insertion/extraction per mole of the oxides. [3] Compared with

* Corresponding author.

E-mail address: weib@udel.edu (B. Wei).

common oxides such as SnO_2 [4], Co_3O_4 [5] and TiO_2 [6], $\alpha\text{-Fe}_2\text{O}_3$ is a more promising anode material with a higher specific capacity over 1000 mAh g^{-1} , three times that of commercial graphite (372 mAh g^{-1}) anodes, as well as a lower cost, higher abundance and more friendliness to environment [7]. In spite of these evident advantages, drawbacks of $\alpha\text{-Fe}_2\text{O}_3$ as anodes are also serious: they would experience structural collapses due to the large volumetric changes during lithiation/delithiation, causing severe capacity degradation and cyclic instability; their inherent low electronic conductivity and poor ionic conductivity owing to $\text{M}_x\text{O}_y/\text{M}^0/\text{Li}_2\text{O}$ matrix deriving from the conversion reactions restrict their rate capability; $\alpha\text{-Fe}_2\text{O}_3$ also suffers from the limited electrochemical kinetics related to the solid-state diffusion of Li ions between electrolyte and electrodes, reflected by the voltage and capacity hysteresis between charge and discharge [7–9].

In order to circumvent these challenges, blending Fe_2O_3 in various nanostructures (particles [10], tubes [7], rods [11], etc.) with carbon additives and binders (polyvinylidene fluoride (PVDF), polytetrafluoroethylene (PTFE) and so on) is a most-used method to process into an electrode film on current collectors. However, it is at the risk of balancing three key factors between conductivity, specific capacity and the adherence of films, i.e. increasing the proportion of carbon additives while reducing that of binders will benefit a prominent conductivity improvement but be unfavorable for a firm attachment of Fe_2O_3 nanomaterials on the current collectors and vice versa. Adding too many these additives will also decrease the specific capacity. In addition, there are template-chemistry strategies using anodic aluminum oxides (AAO) membrane [3] and metal organic frameworks (MOFs) [12] to assist in forming films or growing Fe_2O_3 nanofilms on current collectors with surface modified by chemical etching or electrodeposition techniques to enhance electrochemical performance. However, a good contact between the active materials and current collectors can hardly be stabilized using these methods, which inevitably introduce more interfaces (active materials/inactive materials) [3] and also limit the practical applications at the cost of cumbersome pretreatments and other complex steps.

Single-walled carbon nanotubes (SWNTs) are well-known 1D carbon nanomaterials which are usually employed as ideal scaffolds or substrates to incorporate the extremely-insulating nanostructured active materials, e.g. V_2O_5 [13], $\text{LiNi}_{0.4}\text{Mn}_{0.4}\text{Co}_{0.2}\text{O}_2$ [14], etc. for energy storage device applications owing to their intrinsic superior conductivity, large surface area, robust flexibility and chemical stability. Although high electrochemical performance achieved by these hybrid nanomaterials was attractive, considerable manufacture cost and complicated processing paths consisting of several elaborate steps, e.g. hydrothermal syntheses and post-treatment processes including centrifuging, rinsing, vacuum infiltration to form films are critical factors to be considered.

In this work we present a facile method to obtain uniformly dispersed $\alpha\text{-Fe}_2\text{O}_3$ (<20 nm)/SWNT hybrid films by a simple heat treatment of the as-prepared SWNT macro-films developed in our lab. The SWNT macro-films are the unique films fabricated using a simple chemical vapor deposition (CVD) without any involvement of gaseous or liquid carbon sources (methane, ethylene, xylene, etc.) and catalytic substrates [15]. The SWNT macro-films prove success in enabling fast charge transfer and serving excellent deformable and stretchable buffer layers with strong adhesion to current collectors to inhibit destruction of crystal structure of $\alpha\text{-Fe}_2\text{O}_3$ by accommodating the large volumetric changes during the Li^+ intercalation and deintercalation. The hybrid films as LIB anodes have shown increasingly high specific capacities over 1000 mAh g^{-1} and remarkable cycling stability as long as 100 cycles at different C-rates. We have further investigated the dependence of the Li^+ diffusivity on the film thickness by detailed calculations and analysis of the compatible results

from galvanostatic intermittent titration technique (GITT) and electrochemical impedance spectroscopy (EIS), and found that the $\alpha\text{-Fe}_2\text{O}_3$ /SWNT hybrid films with a comparable thickness to the characteristic diffusion length Li^+ ions shows the optimum electrochemical properties as a promising anode for LIBs.

2. Experimental

2.1. Preparation of $\alpha\text{-Fe}_2\text{O}_3$ /SWNT hybrid films

Single-walled carbon nanotube (SWNT) macro-films were synthesized by the modified floating chemical vapor deposition (CVD) method reported in the previously published work [15]. Briefly, a mixture of ferrocene and sulfur (atomic ratio Fe:S = 1:10, both from Sigma Aldrich) as precursor was heated at 1100–1150 °C in the furnace tube, into which a gas flow of Ar (1500 mL min⁻¹) and H₂ (150 mL min⁻¹) mixture was delivered. Three samples with different thickness were prepared by using 300 mg, 140 mg and 50 mg of the precursors, respectively. Here we name the thickest $\alpha\text{-Fe}_2\text{O}_3$ /SWNT hybrid film as Sample FC_T, the sample with moderate thickness as FC_N and the thinnest one as FC_t. After 10–30 min reaction, the samples were cooled down and the Fe-containing SWNT (Fe/SWNT) macrofilms could be obtained. Then a simple heat treatment of the Fe/SWNT macrofilms at 450 °C in air for 30 min was carried out to obtain the $\alpha\text{-Fe}_2\text{O}_3$ /SWNT hybrid films. When the furnace was cooled down to room temperature, the films were transferred onto the copper foil (9 μm thick) current collectors with the aid of several drops of ethanol to enable a firm adhesion and then the Cu-supported films were punched to 1/2"-disc electrodes after dried in air.

2.2. Characterization

Morphological and structural characterizations were performed using scanning electron microscopy (SEM mode, 3 kV, Zeiss Auriga 60 FIB/SEM) and transmission electron microscope (TEM, JEOL JEM-2010F). X-ray diffraction (XRD, Philips X'Pert diffractometer with Cu K α radiation and a 2θ range of 10–80° with 0.08°/step and 20 s/step) and Raman spectroscopy (Bruker SENTERRA with 532 nm laser excitation) were employed to verify the crystalline structure of the Fe_2O_3 nanoparticles. The thickness of $\alpha\text{-Fe}_2\text{O}_3$ /SWNT hybrid films was measured by optical interferometer (WYKO NT9100, Veeco instrument Inc.) or atomic force microscopy (AFM, SPM Dimension 3100, Veeco instrument Inc.).

2.3. Electrochemical measurements

Before the cell assembly, the total mass of the hybrid films was weighed out using a micro/ultramicro balance (Mettler Toledo XP6) with 0.001 mg accuracy. CR2032 coin cells with the $\alpha\text{-Fe}_2\text{O}_3$ /SWNT hybrid films as working electrodes and lithium ribbons (0.38 mm thick, 99.9%, Sigma–Aldrich) as counter electrodes were assembled in an argon-filled glovebox (MBRAUN UNILab). The Celgard 2500 were chosen as separators and 1 M LiPF₆ dissolved in 1:1 v/v ethylene carbonate (EC): diethyl carbonate (DEC) were obtained from Ferro Co. and used as electrolyte. The cyclic voltammetry curves and electrochemical impedance spectra with a 10 mV AC signal employed from 100 kHz to 10 mHz were all collected by PARSTAT 2273 (Princeton Applied Research) potentiostat/galvanostat. The galvanostatic discharge-charge tests and galvanostatic intermittent titration technique (GITT) were carried out using BT-4, four-channel battery test equipment (Arbin Instrument, Ltd.). GITT measurements consisting of a series of current pulses were applied to the coin cells at a low current of 50 mA g⁻¹ (~0.05 C) for 1 h, each followed by a 10 h rest process. The relaxation time of 10 h was selected to allow full

relaxation of lithium diffusion to reach equilibrium potential and to minimize the self-discharge of $\alpha\text{-Fe}_2\text{O}_3$ during the test.

3. Results and discussion

3.1. Morphological and structural characteristics

Transmission electron microscopy (TEM) demonstrates that the diameter of Fe_2O_3 nanoparticles ranges from 6 to 20 nm (Fig. 1b and right inset) and they are densely distributed at the SWNT-interwoven areas of the as-prepared SWNT macro-films (Fig. 1a). Mean size and size distribution of Fe_2O_3 nanoparticles was determined by PEBBLES free software (<http://pebbles.istm.cnr.it/>) in automatic mode. The selected-area electron diffraction (SAED) patterns in Supplementary Data (SD) convince that $\alpha\text{-Fe}_2\text{O}_3$ nanoparticles with hermatite structure (Fig. S1a) are formed after oxidation of enormous amount of Fe catalysts (Fig. S1b) that came from pyrolysis of ferrocene during CVD reaction in the Fe/SWNT macrofilms. The size of nanoparticles became larger due to the crystal growth during the heat treatment process. Scanning electron microscopy (SEM) images in Fig. 1c and d in a higher magnification display the hybrid films with a uniform morphology and distribution of nanosized Fe_2O_3 particles that well-dispersively decorate the walls of SWNTs. The photograph (inset, Fig. 1d) presents the red/brown semi-transparent appearance of an $\alpha\text{-Fe}_2\text{O}_3$ /SWNT hybrid film.

Powder X-ray diffraction (XRD) pattern (Fig. 2a) shows that Fe catalysts are transformed to rhombohedral $\alpha\text{-Fe}_2\text{O}_3$ phase in *R*-3c

space group, with lattice parameters $a = 5.0347 \text{ \AA}$, $b = 5.0347 \text{ \AA}$, $c = 13.7473 \text{ \AA}$ and $\alpha = \beta = 90^\circ$, $\gamma = 120^\circ$ (JCPDS card no. 01-087-1164). The broad peaks are indicative of $\alpha\text{-Fe}_2\text{O}_3$ nanoparticles in delicate crystalline sizes (10 nm on average) as fine as that observed in the TEM images. Raman spectra show the typical peaks at 225, 248, 290, 400, 490, 600 and 1329 cm^{-1} corresponding to Raman modes of $\alpha\text{-Fe}_2\text{O}_3$ for both the $\alpha\text{-Fe}_2\text{O}_3$ /SWNT hybrid films (black curve) and the pristine $\alpha\text{-Fe}_2\text{O}_3$ after removing SWNTs by heating above 700°C (red curve). [16] The peak at 1589 cm^{-1} in the black spectrum is attributed to G bands of SWNTs [15]. The similar peak positions of the two spectra further confirm the formation of $\alpha\text{-Fe}_2\text{O}_3$. High-resolution TEM (Fig. 3) reveals the crystal lattice fringes of Fe_2O_3 nanoparticles with interplanar distance of 2.69 \AA and 3.62 \AA , which correspond to *d*-spacing of planes (104) and (012), respectively, which are reflected as the most intensive two peaks in the XRD pattern.

Fig. 4a–c shows SEM images with inset photographs of three Cu-supported samples with different thicknesses prepared by adjusting the precursors' amount and CVD deposition time. It is obvious that the thinnest film (Fig. 4c) is almost transparent so that the metal luster of the copper foil at the bottom can be easily observed while the color of the thicker films becomes darker. From Fig. 4a, FC_T, the thickest one out of the three samples has the densest structure where it is scarcely to distinguish individual SWNTs or SWNT bundles. In contrast, SWNTs do not show up to be recognized until the thickness of films is reduced to moderate thickness (FC_N) shown in Fig. 4b and it is easy to identify the long SWNTs entirely wrapped by Fe_2O_3 nanoparticles in the SEM image

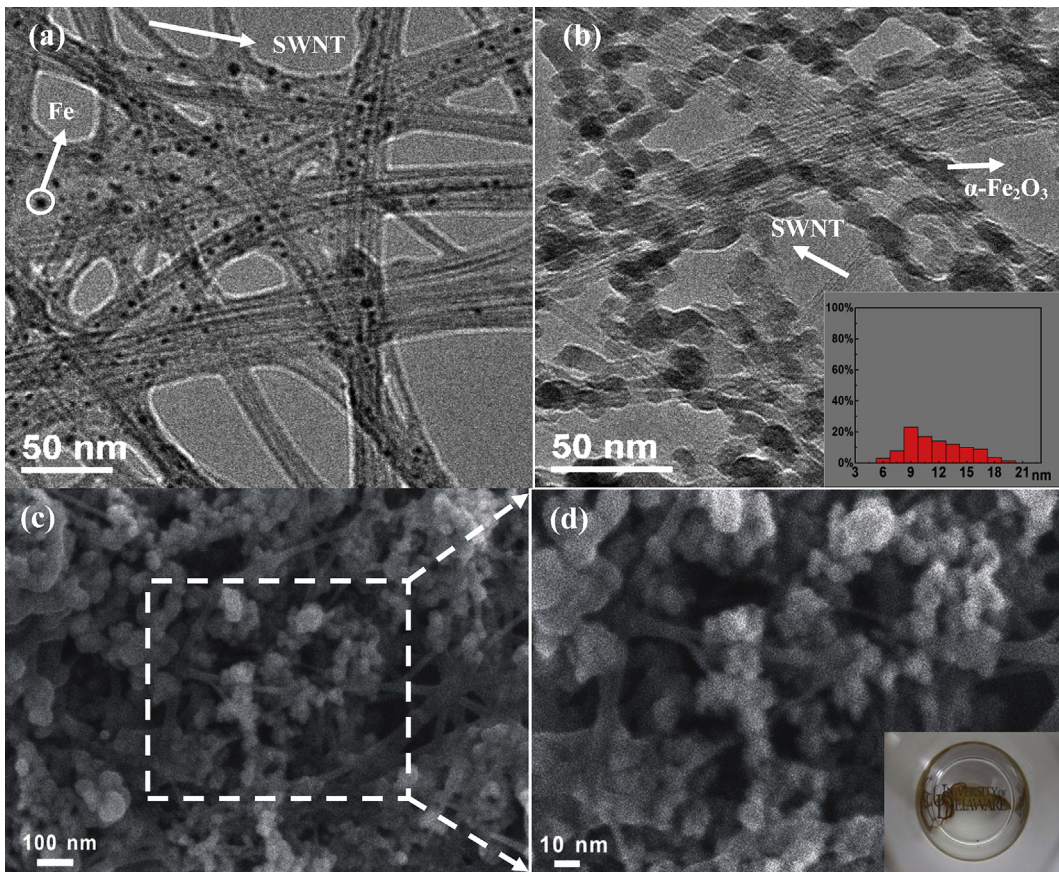


Fig. 1. Microscopy images of SWNT macro-films before and after heat treatment at 450°C in air for 30 min. (a) TEM image of Fe/SWNT macro-film before the heat treatment. (b) TEM image of $\alpha\text{-Fe}_2\text{O}_3$ /SWNT hybrid film and inset: diameter distribution for $\alpha\text{-Fe}_2\text{O}_3$ nanoparticles. (c) SEM image of $\alpha\text{-Fe}_2\text{O}_3$ /SWNT hybrid film. (d) Magnified SEM image of the dashed rectangular area in (c) with an inset: Photograph of a brownish semi-transparent $\alpha\text{-Fe}_2\text{O}_3$ /SWNT hybrid film.

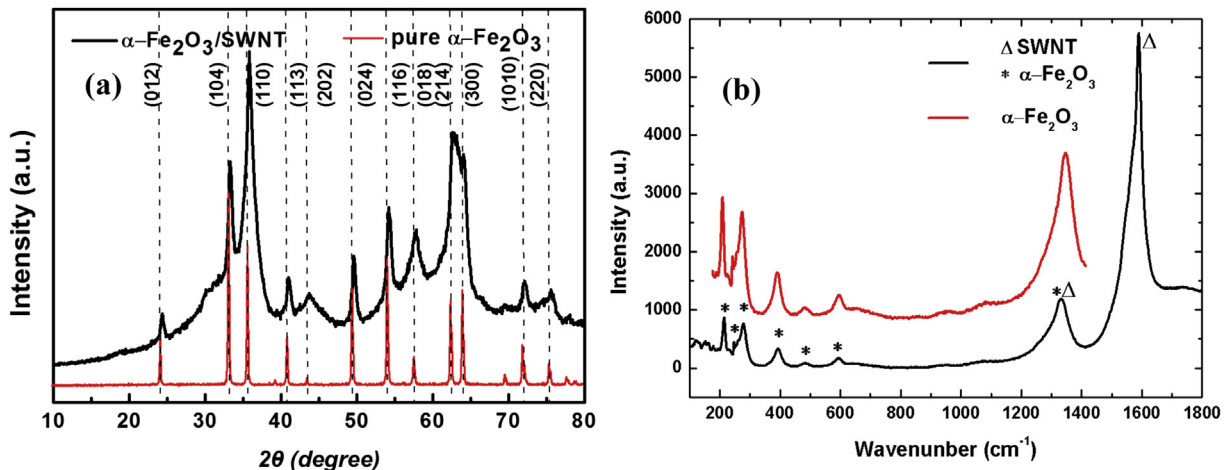


Fig. 2. (a) XRD pattern of $\alpha\text{-Fe}_2\text{O}_3$ /SWNT hybrid films (black) and the pure Fe_2O_3 after removing SWNTs (red). (b) Raman spectra of $\alpha\text{-Fe}_2\text{O}_3$ free of SWNT (red) and $\alpha\text{-Fe}_2\text{O}_3$ /SWNT hybrid film (black). (For interpretation of the references to colour in this figure legend, the reader is referred to the web version of this article.)

of the thinnest sample (FC_t) (Fig. 4c). The thinner films become sparser, particularly for FC_t where the copper substrate underneath is visible. Based on the above information, it was speculated that the thickest hybrid film has the highest concentration of $\alpha\text{-Fe}_2\text{O}_3$. This speculation has been confirmed by the following energy-dispersive X-ray spectroscopy (EDX) mapping results for the three samples with an equally sized area of 5- μm scale (SD, Fig. S2 and the Fe/C weight ratios, Table S1). FC_T has the highest ratio of 10.43:1 compared to 5.38:1 for FC_t and 3.01:1 for FC_N. We hypothesized that an optimal Fe/C weight ratio, which can be reflected by the film thickness, may have a significant impact on the battery performance when the hybrid films are employed as anodes. This point is further confirmed in the electrochemical analysis below.

Fig. 4d manifests that the thickness of FC_T is 5 about μm from the measurement of the average height difference along the line joining the spot marked by B near the edge of film and the flat surface of silicon substrates at A-marked spot by using optical interferometer. Here it is worth to note that the films are adhesively and flat transferred onto the silicon substrate without folding and overlapping by following the same procedures as preparing electrodes (for details see Section 2). Atomic force microscopy (AFM)

images (Fig. 4e and f) show that FC_N and FC_t hybrid films within an area of 5 $\mu\text{m} \times 20 \mu\text{m}$ are about 500 nm and 100 nm thick, respectively by averaging the roughness along the line from spot B on the film to spot A on the silicon surface.

3.2. Electrochemical characteristics

The electrochemical characterizations were conducted for the $\alpha\text{-Fe}_2\text{O}_3$ /SWNT hybrid films with the above-mentioned different thickness as working electrodes in coin cells, which consist of a Li metal foil as the counter electrode and 1 M LiPF₆ in ethylene carbonate (EC) and diethyl carbonate (DEC) (1:1 by volume) as the electrolyte. In a control experiment, the electrode was also prepared by mixing the pure Fe_2O_3 nanoparticles after removing SWNTs from the hybrid films by heating at 700 °C in air for 2 h with carbon black and PVDF binder in a weight ratio of 80:10:10.

Fig. 5a exhibits the discharge-charge curves of FC_T, FC_N and FC_t samples after five cycling tests between 3.0 V and 0.005 V at the current density of 100 mA g⁻¹, compared with those of the pure $\alpha\text{-Fe}_2\text{O}_3$ sample during the first two cycles under the same condition. The voltage plateaus at around 1.5 V, 1.2 V and 0.78 V in the 1st discharge curve of the pure Fe_2O_3 sample represent Li⁺

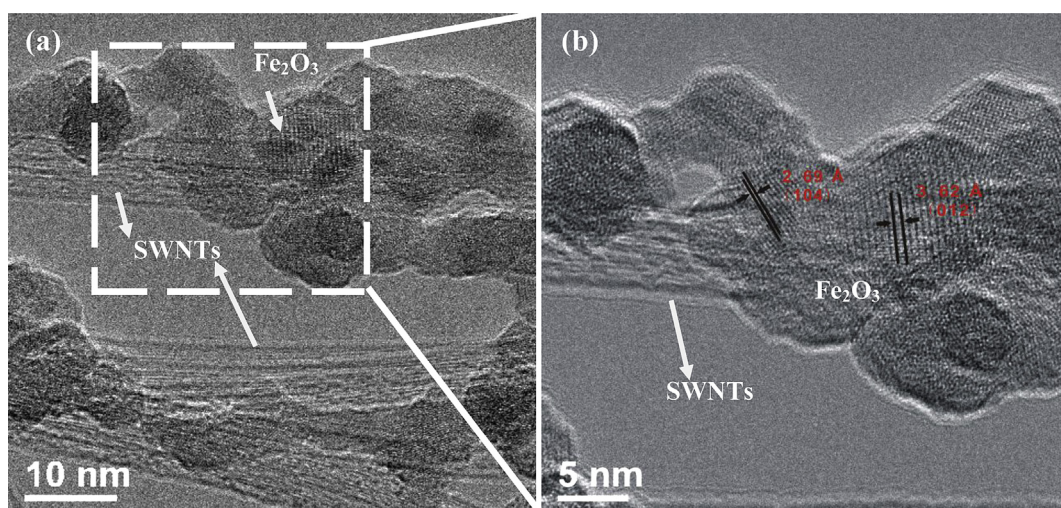


Fig. 3. (a) High-resolution TEM image of $\alpha\text{-Fe}_2\text{O}_3$ /SWNT hybrid films. (b) High-resolution TEM image of dashed rectangular area in (a) with a higher magnification.

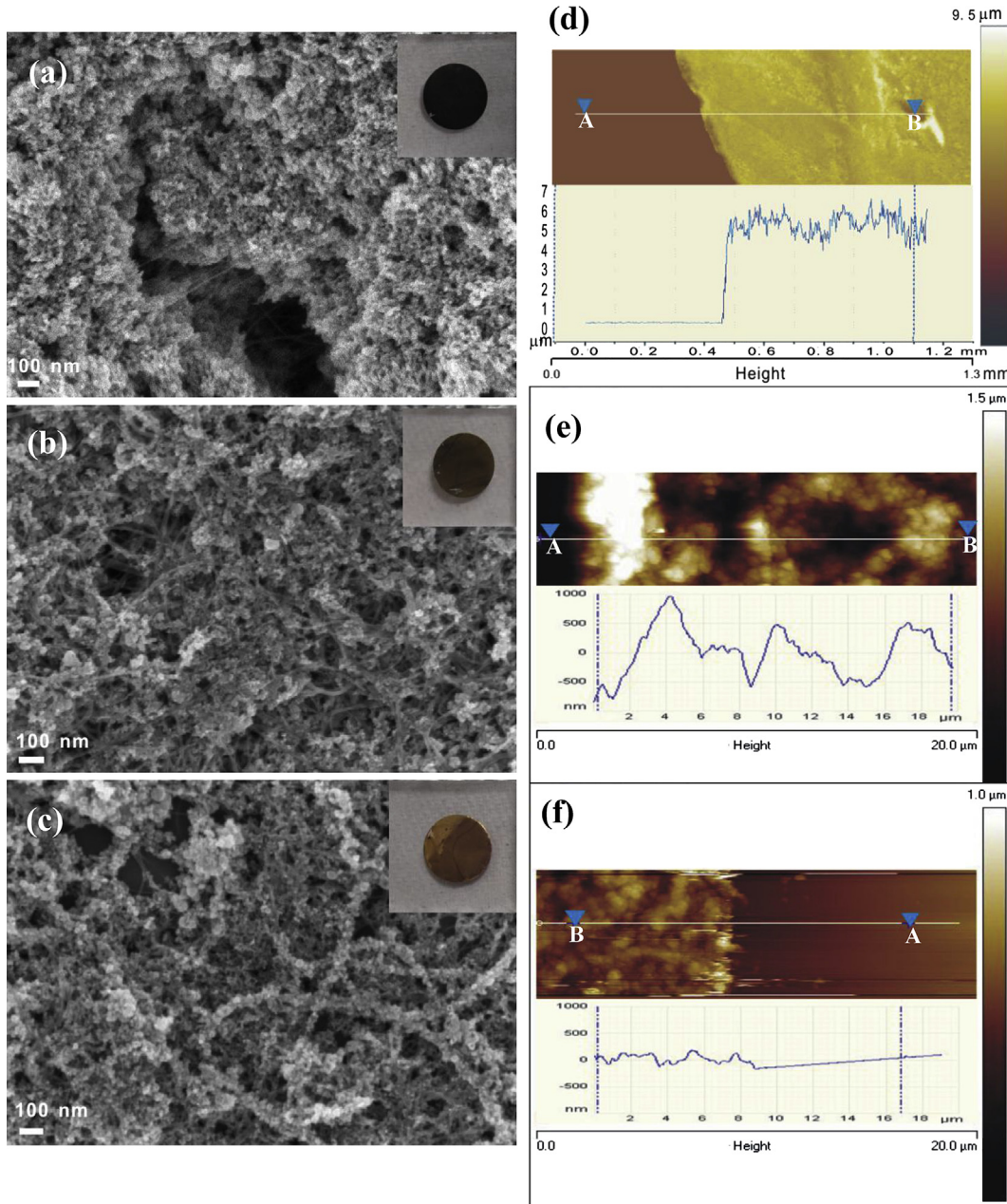
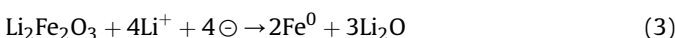
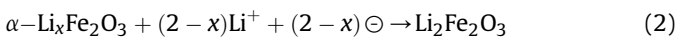
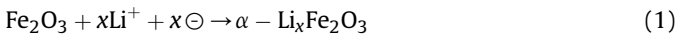
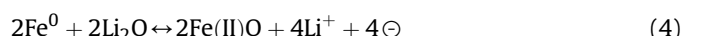


Fig. 4. (a, b, c) SEM images with insets: Photographs of FC_T, FC_N and FC_t, α -Fe₂O₃/SWNT hybrid film samples by sequence. (d) The interferometer image of FC_T with the height information between A and B marked spots. (e, f) The corresponding AFM images of FC_N and FC_t with the roughness measured between A and B marked spots.

intercalation reactions and the conversational reactions, respectively in following equations [7]



while the first charge curve shows a sloping plateau from 1.5 V to 2.2 V, corresponding to the reverse reaction of $\text{Fe}^0 \rightarrow \text{Fe(II)}$ in Eq. (4) [9].



where only 4 moles out of 6 moles Li ions are reversible during the whole cycle, reflected from the charge capacity of 420 mAh g^{-1} compared to 724 mAh g^{-1} for the discharge process (based on the mass of the α -Fe₂O₃ nanoparticles in the mixture). The specific capacity of the pure α -Fe₂O₃ sample in the second cycle decays to 405 mAh g^{-1} only as much as 50% of the initial capacity; that is partly because of the irreversibly structural transformation to co-existed hexagonal α -Li_xFe₂O₃ and cubic Li₂Fe₂O₃ described in Eqs. (1) and (2) [9]. The large volumetric changes of α -Fe₂O₃ arising from such phase transformations also deteriorate the capacity in the sequent cycles. However, the curves from the α -Fe₂O₃/SWNT hybrid films show a longer plateau at a higher voltage of 0.8–0.9 V (the reasons will be explained later) with capacities over 750 mAh g^{-1}

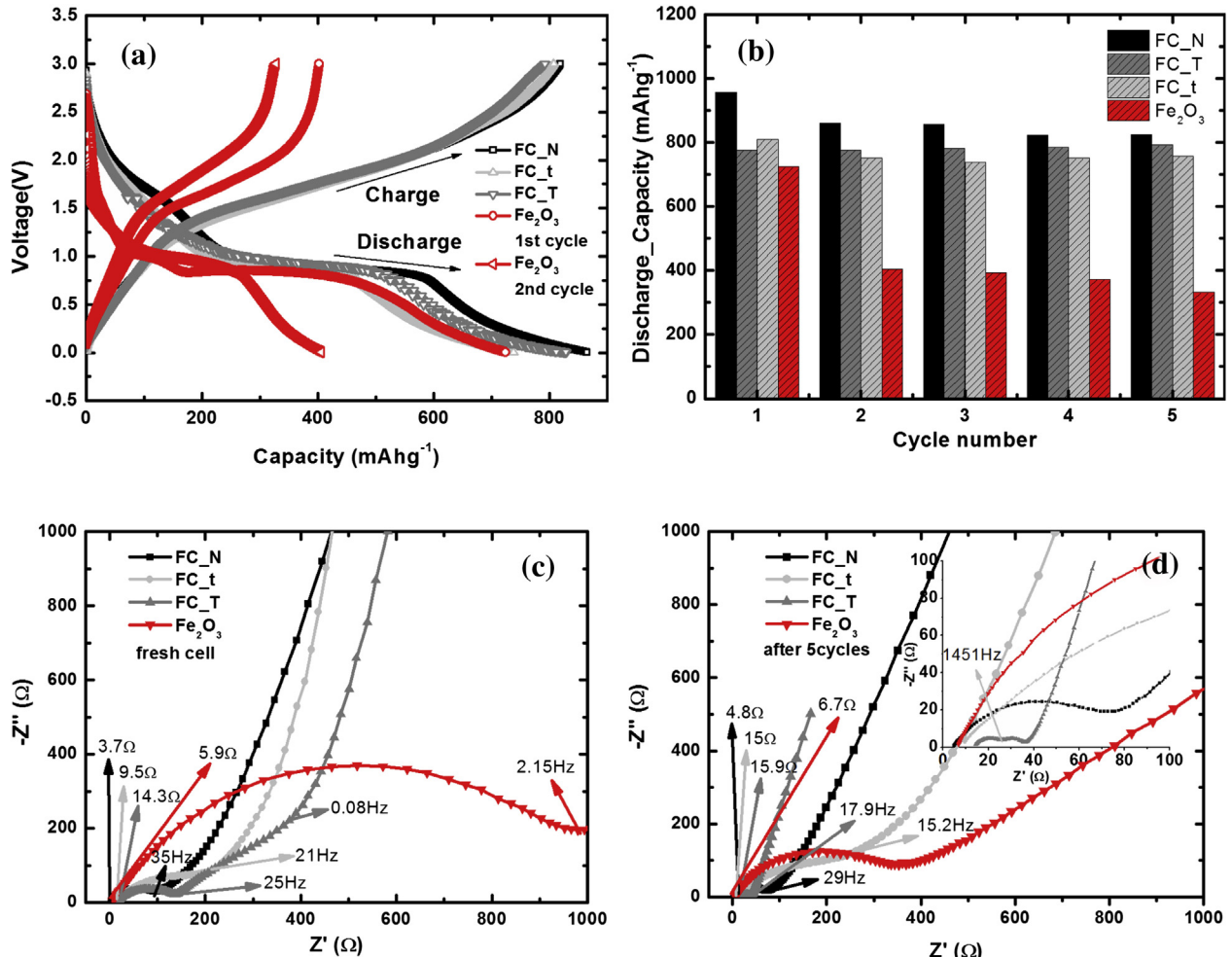


Fig. 5. Electrochemical performance comparison among the four samples: FC_T, FC_N, FC_t and the pure α -Fe₂O₃ free of SWNTs. (a) The galvanostatic discharge-charge curves for the three α -Fe₂O₃/SWNT hybrid film samples at the end of the 5th cycle and the first two cycles of the pure α -Fe₂O₃ sample, all at the same current density of 100 mA g⁻¹. (b) The histogram plot for the discharge specific capacities of all the samples during the five cycles. (c) The Nyquist plots of the as-assembled fresh cells for all the samples. (d) The Nyquist plots of all the samples after five cycling discharge-charge tests at 100 mA g⁻¹.

(FC_t) up to 825 mAh g⁻¹ (FC_N) even after 5 cycles (based on the total mass of the hybrid films). The histogram in Fig. 5b demonstrates that the SWNT macro-films would enhance the specific capacity and the cyclic stability of α -Fe₂O₃ remarkably. On the contrary, α -Fe₂O₃ without SWNTs shows a quick capacity degradation where it degrades from the initial value of 724 mAh g⁻¹ to 332 mAh g⁻¹ with a low retention of less than 46% for five cycles. Among the α -Fe₂O₃/SWNT hybrid films, FC_N has the highest discharge capacity during the first five cycles, and this is related to the thickness we will discuss later.

EIS analysis has been performed in order to elucidate the difference in the electrochemical performance of the four samples from the viewpoint of electrochemical kinetics. The Nyquist plots of the fresh cells before the cyclic tests in Fig. 5c show that FC_N has the smallest series resistance (R_s) involving electrode, electrolyte and their contact interface. The smallest R_s may results from the lowest Fe/C ratio the sample FC_N owns. All the hybrid films show the semicircles with much shorter arc length than the pure Fe₂O₃ sample. The hybrid films have much smaller charge-transfer resistance (R_{ct}) extrapolated from the real-impedance intersection of semicircle at intermediate frequency of 35 Hz for FC_N, 25 Hz for FC_T and 21 Hz for FC_t than the R_{ct} at 2.15 Hz for the pure Fe₂O₃ sample without SWNTs [17], indicating SWNTs contribute greatly

to the improvement of the conductivity. The smallest R_{ct} at the highest frequency means that FC_N has the fastest charge-transfer process which could be optimized by Fe/C weight ratio, i.e. by controlling the thickness of α -Fe₂O₃/SWNT hybrid films. From Fig. 5c, we can also find that approximately 45° Warburg line of FC_T is the longest among the three hybrid film samples probably due to the onset of finite length effects originating from the highest concentration of Fe₂O₃ [18]. Thus, FC_T has the largest limiting resistance (R_L) extrapolated from the interception of capacitive line at the intersection of the Warburg and capacitive lines to the real impedance axis in the Nyquist plot [18]. The larger R_L to describe the Li⁺ diffusion materials demotes the worse diffusive kinetics they possess [18]. The largest R_L for FC_T may come from the narrowing pore sizes of the densest architecture as shown in Fig. 4a. Fig. 5d shows that the R_s for all samples are increased after five cycles and the arc lengths of semicircles for all samples become shorter, i.e. reduced R_{ct} , as a result of the stable solid electrolyte interface (SEI) formation [11]. The convergence linking the semicircle with the Warburg line for the hybrid films all shifts towards the lower frequency (ω_C), indicating the slowing kinetics during cycling which also explains the capacity fading for FT_N and FT_t. However, it is obviously found that the single semicircle for FC_T fresh cell is separated into two converged at high frequency of

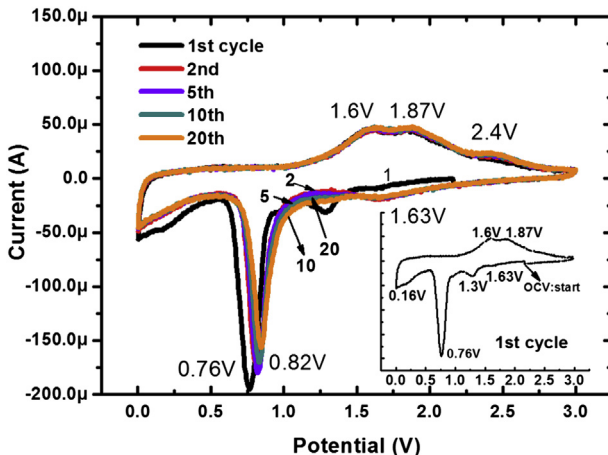


Fig. 6. Selected cycle curves from cyclic voltammetry of the FC_500 (~ 500 nm thick) α -Fe₂O₃/SWNT hybrid film sample between 0 and 3 V at a scan rate of 0.1 mV s^{-1} for 20 cycles. Numbers represent the cycle number. Potentials of peaks are also labeled.

1451 Hz from the magnified high frequency part of the inset of the Nyquist plot after five cycles. This may be caused by the splitting of α -Fe₂O₃ nanoparticles far away from the SWNT surfaces off the hybrid films [19]. The front semicircle at higher frequency is

attributed to the intimately-anchored Fe₂O₃/SWNT integrity with a super high kinetics (1451 Hz) which could offset the diminishing of ω_C and stabilize the capacity of FC_T as cycle goes, contrary to FT_N and FT_t as shown in Fig. 5b.

The electrochemical behavior of 500 nm thick α -Fe₂O₃/SWNT hybrid film (FC_N) has shown the best electrochemical performance out of three and was thoroughly investigated.

Cyclic voltammetry (CV) was carried out in the range from 0 to 3 V at a scan rate of $100 \mu\text{V s}^{-1}$ for 20 cycles. The results of the first cycle, 2nd, 5th, 10th and the last cycle are shown in Fig. 6. The cathodic peaks at 1.63 V and 1.3 V in the 1st sweep starting with an open circuit voltage (OCV, 2.2 V) are ascribed to the single hexagonal phase by Li⁺ insertion and the occurrence of another Li-intercalated phase, cubic Li₂Fe₂O₃, as described in Eqs. (1) and (2). The sharp peak at 0.76 V with the highest cathodic current is assigned to the reduction of Fe(II) ions Li₂Fe₂O₃ to Fe⁰, corresponding to Eq. (3). In the other half-cycle process (anodic) of the first sweep, two adjacent anodic peaks mirror-symmetrical to each other (twin peaks) at 1.6 V and 1.87 V derive from a two-step Li⁺ reversible charge reaction of $\text{Fe}^0 \rightarrow \text{Fe}(\text{II})$ as shown in Eq. (4) [9]. In the subsequent CV measurements from the second cycle up to 20 cycles, cathodic peak at 1.63 V becomes more prominent while the one at 1.3 V, well defined in the first cathodic sweep, is absent, probably owing to the combined effect of the irreversibility of Eq. (2) with the reduction from Li₂Fe₂O₃ to Fe⁰ [20]. The major cathodic peaks corresponding to $\text{Fe}(\text{II}) \rightarrow \text{Fe}^0$ all shift to a higher potential at

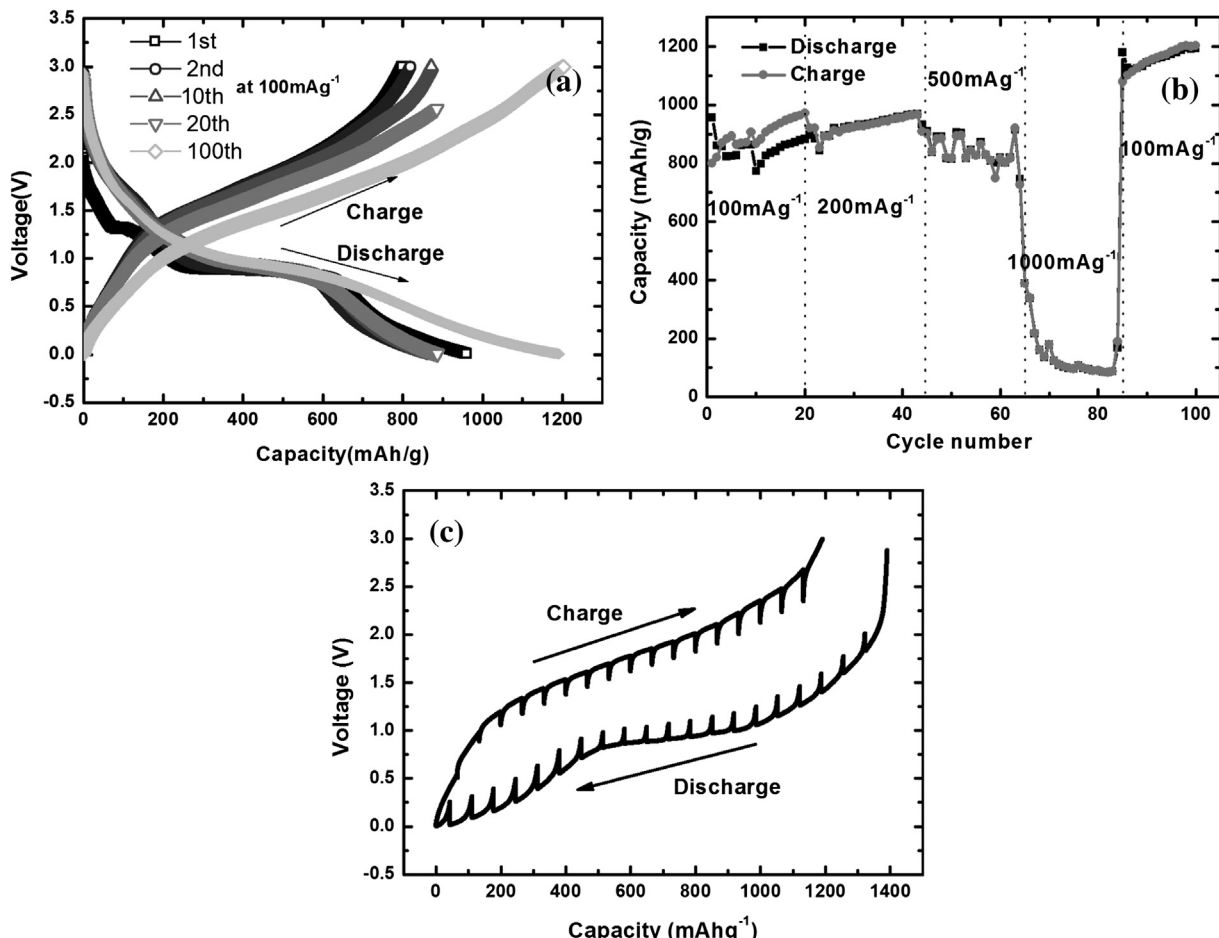


Fig. 7. Electrochemical measurements of a half-cell composed of FC_500 sample and Li. The specific capacities are based on the total mass of the hybrid films. (a) The galvanostatic discharge–charge curves at the same current density of 100 mA g^{-1} for the 1st, 2nd, 10th, 20th and 100th cycle. (b) Capacity retention of FC_500 at various current densities. (c) The GITT curve of FC_500 plotted as voltage VS capacity.

0.82 V with a lower current compared to the peak at 0.76 V in the first cycle. This may be caused by the irreversible phase transformation accomplished after the first cycle, i.e. addition of cubic-phase $\text{Li}_2\text{Fe}_2\text{O}_3$. On the contrary, the twin anodic peaks remain at 1.6 and 1.87 V, indicating the good reversibility of $\text{Fe}^0 \rightarrow \text{Fe(II)}$. The new-born anodic peak at 2.4 V may be attributed to a deeper oxidation of $\text{Fe(II)} \rightarrow \text{Fe(III)}$ [20]. In addition, the well-overlapped curves after the first cycle manifest the good cyclic stability of FC_N as anodes.

Galvanostatic discharge-charge cycling measurements have been performed to evaluate the capacity retention and the cyclic stability of cell at various current densities of 100 mA g^{-1} , 200 mA g^{-1} , 500 mA g^{-1} and 1000 mA g^{-1} for 100 cycles in total. The voltage profiles for the selected cycles in the 1st, 2nd, 10th, 20th and 100th at the same rate of 100 mA g^{-1} are shown in Fig. 7a. The discharge curve for the 1st cycle shows the shortest voltage plateau at 1.7 V followed by the longer one at 1.3 V and the longest at 0.8 V, which represent the same processes as the Eqs. (1)–(3) indicated. From the 2nd cycle to the 20th cycle, the discharge curves have a sloped plateau at $\sim 1.6 \text{ V}$ and then an extended voltage plateau at elevated potential $\sim 0.9 \text{ V}$ compared to the 1st cycle while the charge curves have a similar potential to the first cycle between 1 V and 2.2 V. These results coincide well with CV analysis discussed above. When cycle reached the 100th, the shorter voltage plateau around 1.6 V is absent in the discharge profile. Instead, there is a single one at the potential around 1 V increased by 0.1 V while the charge potential is decreased by about 0.2 V, rendering a lower overpotential (by about 0.3 V). Fig. 7b shows the specific capacity of FC_N during 100 cycles at different rates. The cell was first cycled at 100 mA g^{-1} for 20 cycles where the specific discharge capacity of

956 mAh g^{-1} initially delivered declines to 795 mAh g^{-1} at the end of the 10th cycle and then rebounds constantly with an overall average capacity of 852 mAh g^{-1} . Continuously, when the current density was increased to 200 mA g^{-1} , the cell keeps at a stable capacity of 927 mAh g^{-1} and the Coulombic efficiency is improved from the mean value of 91% within the first 10 cycles to 99.7% since the 20th cycle. The rise in capacity and Coulombic efficiency may be attributed to transition from Li^+ intercalation mechanism to the reversible $\text{Fe}^0 \leftrightarrow \text{Fe(III)}$ conversional reactions through the deeper oxidation of $\text{Fe(II)} \rightarrow \text{Fe(III)}$ since the 10th cycle. The cell performance at 500 mA g^{-1} shows a fluctuating capacity of 850 mAh g^{-1} on average and it drops below 200 mAh g^{-1} quickly at a high current density of 1000 mA g^{-1} . This result indicates a low rate capability which is limited by the extremely slow kinetics of $\alpha\text{-Fe}_2\text{O}_3$ nanoparticles themselves despite the improvement by SWNT macro-films. The fluctuation was also as a result of the severe structural transformation during Li^+ insertion and extraction from $\alpha\text{-Fe}_2\text{O}_3$ at high current density. After deep cycling at 1000 mA g^{-1} , an increasing capacity over 1100 mAh g^{-1} can be restored when returning the current density to 100 mA g^{-1} , exhibiting an excellent cyclic stability. It is proposed that the capacity increase over the theoretical capacity calculated from $\text{Fe}^0 \leftrightarrow \text{Fe(II)}$ transition by in the last 15 cycles could result from the relaxation of electrochemical activation and the further reversible $\text{Fe}^0 \leftrightarrow \text{Fe(III)}$ conversional reactions [21].

In order to confirm this as well as to better understand the nature of kinetic properties of the $\alpha\text{-Fe}_2\text{O}_3$ /SWNT hybrid films, GITT is employed to analyze the Li-ion transport kinetics for the mixed-conducting electrodes by using a small constant current, and measuring potential changes as a function of time [22] (see

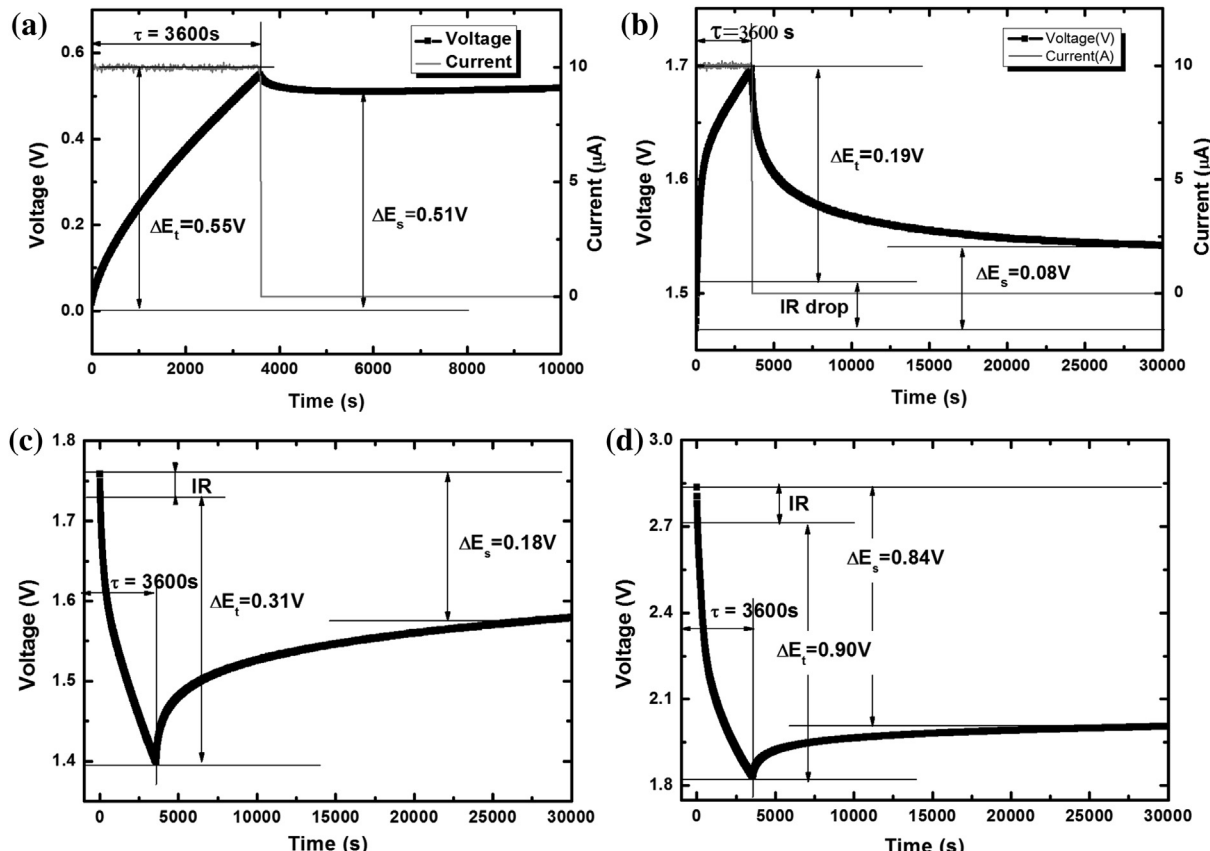


Fig. 8. Polarized curves for current pulse steps from GITT data at various potentials in discharge and charge processes. (a, b) Upon charge, 0–0.6 V and 1.5–1.7 V. (c, d) Upon discharge, 1.8–1.4 V and 3–1.8 V.

details in Section 2). From Fig. 7c, the specific charge capacity of FC_500 can achieve 1200 mAh g⁻¹ and the discharge capacity is as high as 1400 mAh g⁻¹ due to the fully Li⁺ diffusive reactions given the relaxation time is sufficient to allow the system to reach equilibrium. The discharge process shows a voltage plateau at around 1 V arising from the reduction of Fe(II) to Fe⁰ and the inclined tail part below 0.5 V may come from the contribution of SWNTs with a capacity of 380 mAh g⁻¹ (theoretical capacity for graphite is 372 mAh g⁻¹). The equilibrium voltage upon charge shows a sharp slope up to 200 mAh g⁻¹ which originates from SWNTs, followed by a longer increased slope from 1.2 V to 2.8 V, indicating that the Li removal might proceed as a continuous Fe⁰ → Fe(II) → Fe(III) reaction. These results are in good agreement with the analysis above and consequently confirm our supposition on the reasons for the capacity increment.

The effective Li⁺ chemical diffusion coefficient can be determined by GITT, using Fick's law through the following equation (Eq. (5)) [22]

$$D_{\text{GITT}} = \frac{4}{\pi\tau} \left(\frac{m_b V_M}{M_b S} \right)^2 \left(\frac{\Delta E_s}{\Delta E_t} \right)^2 \quad (\tau \ll L^2/D_{\text{GITT}}) \quad (5)$$

where L is the characteristic length; S is the contact area between the electrode and electrolyte; V_M is the molar volume of the electrode material; M_b and m_b are the atomic weight of b and the mass of the component b in the sample; ΔE_t is the total change of the cell voltage during the current pulse for the time τ , neglecting the IR drop due to the current flux through the electrolyte and the interface; ΔE_s is the change of the steady-state voltage of the cell for the step in different potential range as illustrated and defined in Fig. 8 (pulse steps at different potentials in the discharge-charge cycle). [22] Here the component b is $\alpha\text{-Fe}_2\text{O}_3$ and we simplify the V_M as the molar volume of pure $\alpha\text{-Fe}_2\text{O}_3$ because its high concentration over 80% in the hybrid films (SD, Table S1). V_M can be calculated from Eq. (6) as follows [23]:

$$V_M = N_A \frac{V_{\text{cell}}}{Z} \quad (6)$$

where V_{cell} is the unit cell volume; N_A is Avogadro constant and Z is the number of formula units in the unit cell. V_{cell} is calculated from the unit cell parameters of $\alpha\text{-Fe}_2\text{O}_3$ in rhombohedral representation (SD, Fig. S3).

The polarization curves in Fig. 8a and b are representative of each step at around 0.2 V and 1.5 V, respectively during the charge process. When the cell goes to a higher voltage upon charging, it needs more time for relaxation of pulse to reach a steady state or unable to reach. On the contrary, the relaxation time of pulse would be delayed when the cell is discharged to lower voltage (Fig. 8c and d). These phenomena reflect the change of lithium diffusion coefficients during different process at various voltages. The overpotential, i.e., the voltage difference between equilibrium potential at the end of relaxation and the potential at the end of the current pulse ($\approx \Delta E_t - \Delta E_s$, neglecting the IR drop) [24] increases as both charge and discharge proceed. Thus, the potential hysteresis could be maintained as shown by GITT in Fig. 7c.

In the subsequent analysis, we relied on EIS measurements to calculate the Li⁺ chemical diffusion coefficients at different potentials to make a comparison with those as determined by GITT in order to clarify the potential relationship between the film thickness and the Li⁺ diffusivity and consequently the difference in cell performance for the hybrid films with different thicknesses. Given by the thickness of 500 nm and EIS results for FC_500 (Fig. 9a and b), Li⁺ diffusion coefficient can be calculated according to the following equations [25]:

$$D_{\text{EIS}} = \frac{t^2}{4\tau} \quad (7)$$

$$\tau = 2 \left(\frac{Q_m \sigma dx}{dE} \right)^2 = 2C_{\text{int}}^2 \sigma^2 \quad (8)$$

$$C_{\text{int}} = \frac{Q_m dx}{dE} \quad (9)$$

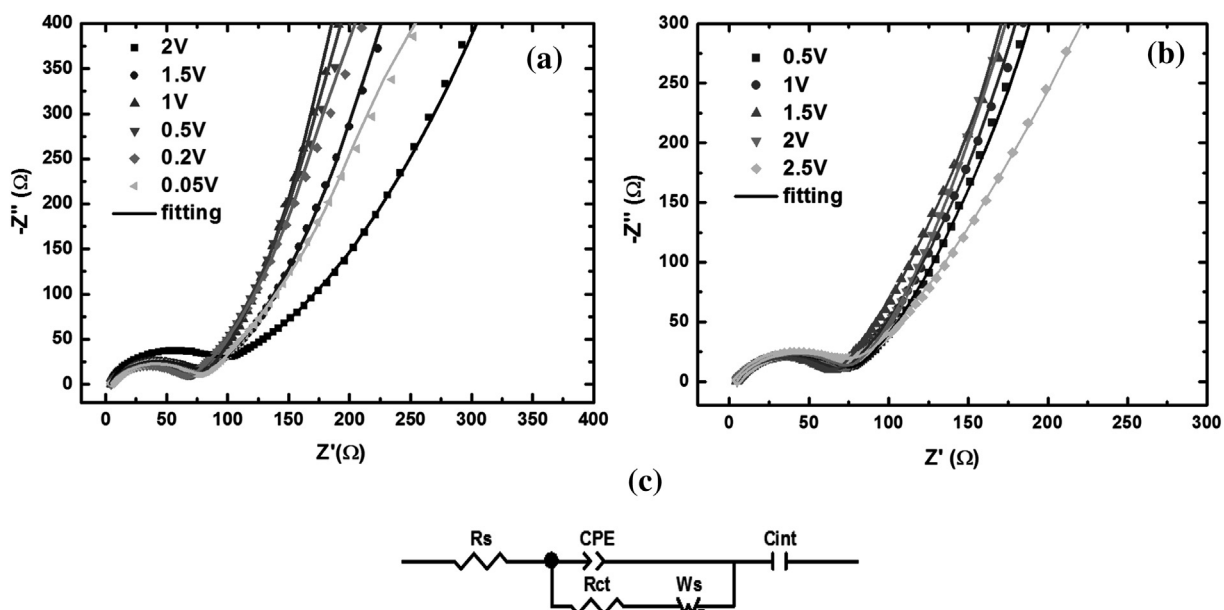


Fig. 9. Electrochemical impedance spectra for FC_500. (a, b) Nyquist plots at various potentials and the corresponding fitting lines upon discharge and charge. (c) Equivalent circuit model employed in the curve fitting.

Table 1

The fitting values of components in equivalent circuit for Fig. 9a.

Potential at discharging (V)	Series resistance, $R_s (\omega)$	Charge transfer resistance, $R_{ct} (\omega)$	Warburg impedance, $W_s (\omega)$	Constant phase element, CPE (F)	Intercalation capacitance, C_{in} (F)
2	3.722	83.9	38.13	1.9054E-5	0.0050175
1.5	4.11	72.28	36.71	4.9431E-5	0.013473
1	4.351	70.15	39.74	5.1375E-5	0.015545
0.5	4.282	62.91	58.62	5.224E-5	0.026113
0.2	4.385	61.31	54.86	6.2949E-5	0.032586
0.05	4.51	72.19	62.21	7.6176E-5	0.061731

$$\sigma = \frac{Z''}{\omega^{-\frac{1}{2}}} \quad (\omega \rightarrow 0) \quad (10)$$

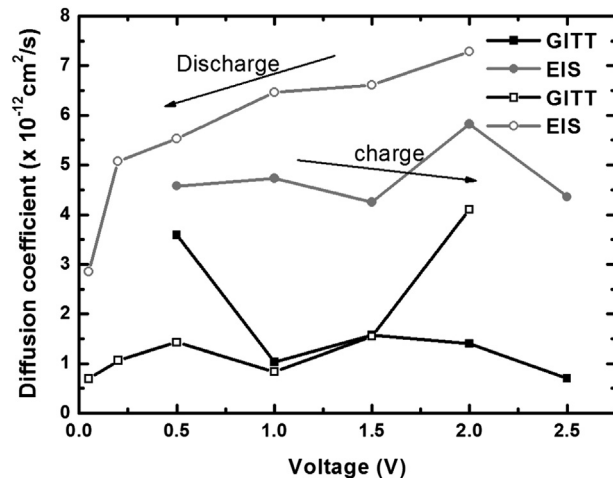
where t is the film thickness; τ is characteristic diffusion time and σ is the Warburg coefficient; Q_m is the total inserted Li ions and dE/dx is the slope of the coulometric titration curve; C_{int} is capacitance for Li^+ diffusion; Z'' is the imaginary impedance and ω is the angular frequency [25]. C_{int} can be obtained by fitting the EIS data recorded during discharge (Fig. 9a) and charge (Fig. 9b) at various potentials with the corresponding equivalent circuits (ECs) as shown in Fig. 9c. Tables 1 and 2 list the fitting values of components in ECs. Warburg coefficient σ is extrapolated by fitting the slope of curve (Z'' versus the square root of ω at low frequency). The values of σ at various potentials are listed with the diffusion coefficients D_{EIS} in Tables S2 and S3, SD.

The results of Li^+ chemical diffusion coefficients calculated from the EIS (D_{EIS}) and GITT (D_{GITT}) are shown in Fig. 10. The overall tendency of the variation for both D_{EIS} and D_{GITT} is basically in decrement as the charge and discharge proceed, which also coincides with that of Warburg impedance W_s (Tables 1 and 2) and the results of polarization curves as described in Fig. 8. D_{EIS} in the range of 3×10^{-12} – $7 \times 10^{-12} \text{ cm}^2 \text{ s}^{-1}$ is a little higher than D_{GITT} ranging from 1×10^{-12} – $4 \times 10^{-12} \text{ cm}^2 \text{ s}^{-1}$ probably due to the insufficient equilibrium confined by the characteristic diffusion length L for the EIS measurements. Therefore, the hybrid films with the thickness of 300–500 nm, which is comparable to the characteristic diffusion length, L , may have the optimal electrochemical performance. If the hybrid film was too thick or too thin, it would not benefit the maximization of Li^+ diffusivity for $\alpha\text{-Fe}_2\text{O}_3$ nanoparticles. Thus, it is no wonder that the cell with FC_500 films closest to 300–500 nm thick has an excellent performance in terms of the highest specific capacity and the cyclic stability. However the Li^+ chemical diffusion coefficient with a factor of –12 is too low and is responsible for the inferior rate performance described above. This remains a challenge to overcome in the future work.

Table 2

The fitting values of components in equivalent circuit for Fig. 9b.

Potential at discharging (V)	Series resistance, $R_s (\omega)$	Charge transfer resistance, $R_{ct} (\omega)$	Warburg impedance, $W_s (\omega)$	Constant phase element, CPE (F)	Intercalation capacitance, C_{in} (F)
0.5	4.207	71.29	73.99	8.5774E-5	0.03205
1	5.184	62.13	53.81	6.0959E-5	0.029044
1.5	4.418	60	39.23	6.1094E-5	0.025756
2	4.479	68.64	53.91	5.9489E-5	0.013761
2.5	4.478	73.38	33.83	6.8308E-5	0.010591

**Fig. 10.** Li^+ chemical diffusion coefficients of FC_500 determined by GITT and EIS during charge and discharge processes.

4. Conclusions

In conclusion, we have demonstrated a novel $\alpha\text{-Fe}_2\text{O}_3$ /SWNT hybrid film obtained by a simple heat treatment method that exhibits enhanced electrochemical properties of $\alpha\text{-Fe}_2\text{O}_3$ and as a promising anode material for rechargeable lithium-ion batteries. The SWNT macro-films with a high conductivity and flexibility can remarkably facilitate the electrochemical kinetics and buffer the strains caused by Li-intercalated phase transformation to improve the specific capacity and cyclic stability of $\alpha\text{-Fe}_2\text{O}_3$ anodes. The hybrid film anodes can take the best of reversible $\text{Fe}^0 \leftrightarrow \text{Fe(III)}$ conversion reactions to approach the theoretical capacity of $\alpha\text{-Fe}_2\text{O}_3$ over 1000 mAh g^{-1} . The $\alpha\text{-Fe}_2\text{O}_3$ /SWNT hybrid films with the thickness that comparable to the characteristic diffusion length of 300–500 nm has the highest Li^+ chemical diffusion coefficient and thus possesses an optimal electrochemical performance in terms of the highest specific capacity and the cyclic stability. The findings reported here will provide a strategy to develop the hybrid nanostructured metal oxides and carbon nanomaterials as high-performance electrodes for thin film lithium ion batteries.

Acknowledgments

This work was financially supported by the US national science foundation (NSF) under the contract of 1067947.

Appendix A. Supplementary data

Supplementary data related to this article can be found at <http://dx.doi.org/10.1016/j.jpowsour.2013.04.101>.

References

- [1] M. Armand, J.M. Tarascon, Nature 451 (2008) 652–657.
- [2] J.M. Tarascon, M. Armand, Nature 414 (2001) 359–367.
- [3] P.L. Taberna, S. Mitra, P. Poizot, P. Simon, J.M. Tarascon, Nat. Mater. 5 (2006) 567–573.
- [4] N. Li, C.R. Martin, B.A. Scrosati, Electrochim. Solid-State Lett. 3 (2000) 316–318.
- [5] Y. Li, B. Tan, Y. Wu, Nano Lett. 8 (2007) 265–270.
- [6] D. Wang, D. Choi, J. Li, Z. Yang, Z. Nie, R. Kou, D. Hu, C. Wang, L.V. Saraf, J. Zhang, I.A. Aksay, J. Liu, ACS Nano 3 (2009) 907–914.
- [7] J. Chen, L. Xu, W. Li, X. Gou, Adv. Mater. 17 (2005) 582–586.
- [8] D. Larcher, C. Masquelier, D. Bonnin, Y. Chabre, V. Masson, J.-B. Leriche, J.-M. Tarascon, J. Electrochim. Soc. 150 (2003) A133–A139.

- [9] M.V. Reddy, T. Yu, C.H. Sow, Z.X. Shen, C.T. Lim, G.V. Subba Rao, B.V.R. Chowdari, *Adv. Funct. Mater.* 17 (2007) 2792–2799.
- [10] X. Zhu, Y. Zhu, S. Murali, M.D. Stoller, R.S. Ruoff, *ACS Nano* 5 (2011) 3333–3338.
- [11] Y.-M. Lin, P.R. Abel, A. Heller, C.B.J. Mullins, *Phys. Chem. Lett.* 2 (2011) 2885–2891.
- [12] X. Xu, R. Cao, S. Jeong, J. Cho, *Nano Lett.* 12 (2012) 4988–4991.
- [13] M. Sathiya, A.S. Prakash, K. Ramesha, J.M. Tarascon, A.K. Shukla, *J. Am. Chem. Soc.* 133 (2011) 16291–16299.
- [14] C. Ban, Z. Li, Z. Wu, M.J. Kirkham, L. Chen, Y.S. Jung, E.A. Payzant, Y. Yan, M.S. Whittingham, A.C. Dillon, *Adv. Energ. Mater.* 1 (2011) 58–62.
- [15] H. Zhu, B. Wei, *Chem. Commun.* (2007) 3042–3044.
- [16] A. Nasibulin, S. Rackauskas, H. Jiang, Y. Tian, P. Mudimela, S. Shandakov, L. Nasibulina, S. Jani, E. Kauppinen, *Nano Res.* 2 (2009) 373–379.
- [17] A.J. Bard, L.R. Faulkner, *Electrochemical Methods – Fundamentals and Applications*, Wiley, Hoboken, 2001.
- [18] C. Ho, I.D. Raistrick, R.A. Huggins, *J. Electrochem. Soc.* 127 (1980) 343–350.
- [19] Z.Y. Cao, B.Q. Wei, *Nano Energy* (2012), <http://dx.doi.org/10.1016/j.nanoen.2012.11.013>.
- [20] J. Morales, L. Sánchez, F. Martín, F. Berry, X. Ren, *J. Electrochem. Soc.* 152 (2005) A1748–A1754.
- [21] P. Poizot, S. Laruelle, S. Gruegeon, L. Dupont, J.M. Tarascon, *Nature* 407 (2000) 496–499.
- [22] W. Weppner, R.A. Huggins, *J. Electrochem. Soc.* 124 (1977) 1569–1578.
- [23] I. Mills, T. Cvita, K. Homann, N. Kallay, K. Kuchitsu, in: *Quantities, Units and Symbols in Physical Chemistry*, second ed., Blackwell Science Ltd, Oxford, 1993.
- [24] Y. Zhu, C. Wang, *J. Power Sources* 196 (2011) 1442–1448.
- [25] M.D. Levi, G. Salitra, B. Markovsky, H. Teller, D. Aurbach, U. Heider, L. Heider, *J. Electrochem. Soc.* 146 (1999) 1279–1289.